Supporting Information

Interparticle Interaction-Dependent Jamming in Colloids: Insights into Glass

Transition and Morphology Modulation during Rapid Evaporation-Induced Assembly

Swati Mehta[1,3], Jitendra Bahadur[1,3]*, Sandeep K. Sharma[2,3], Debasis Sen[1,3]

[1]Solid State Physics Division, Bhabha Atomic Research Centre, Mumbai 400085, India

[2]Radiochemistry Division, Bhabha Atomic Research Centre, Mumbai, 400085, India

[3]Homi Bhabha National Institute, Anushaktinagar, Mumbai 400094, India

1. Size distribution of SM30 and TM40 obtained through the fitting of SAXS profiles
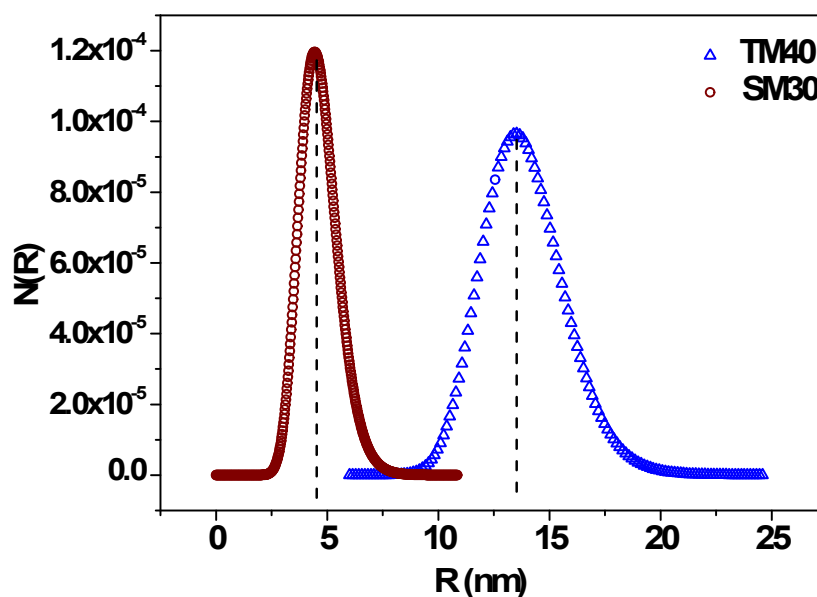

Figure S1: *The size distribution of SM30 and TM40 nanoparticles obtained via the model-dependent fitting of the SAXS profiles.*

In general particle size distribution is estimated from the scattering profile of the dilute sample where the S(Q)→1. For concentrated colloids with moderate size polydispersity, the fitting of

the scattering profile under local monodisperse approximation provides an estimation of the particle size distribution

2. Thermogravimetric Analysis (TGA) and Fourier Transform Infrared Spectroscopy (FTIR)
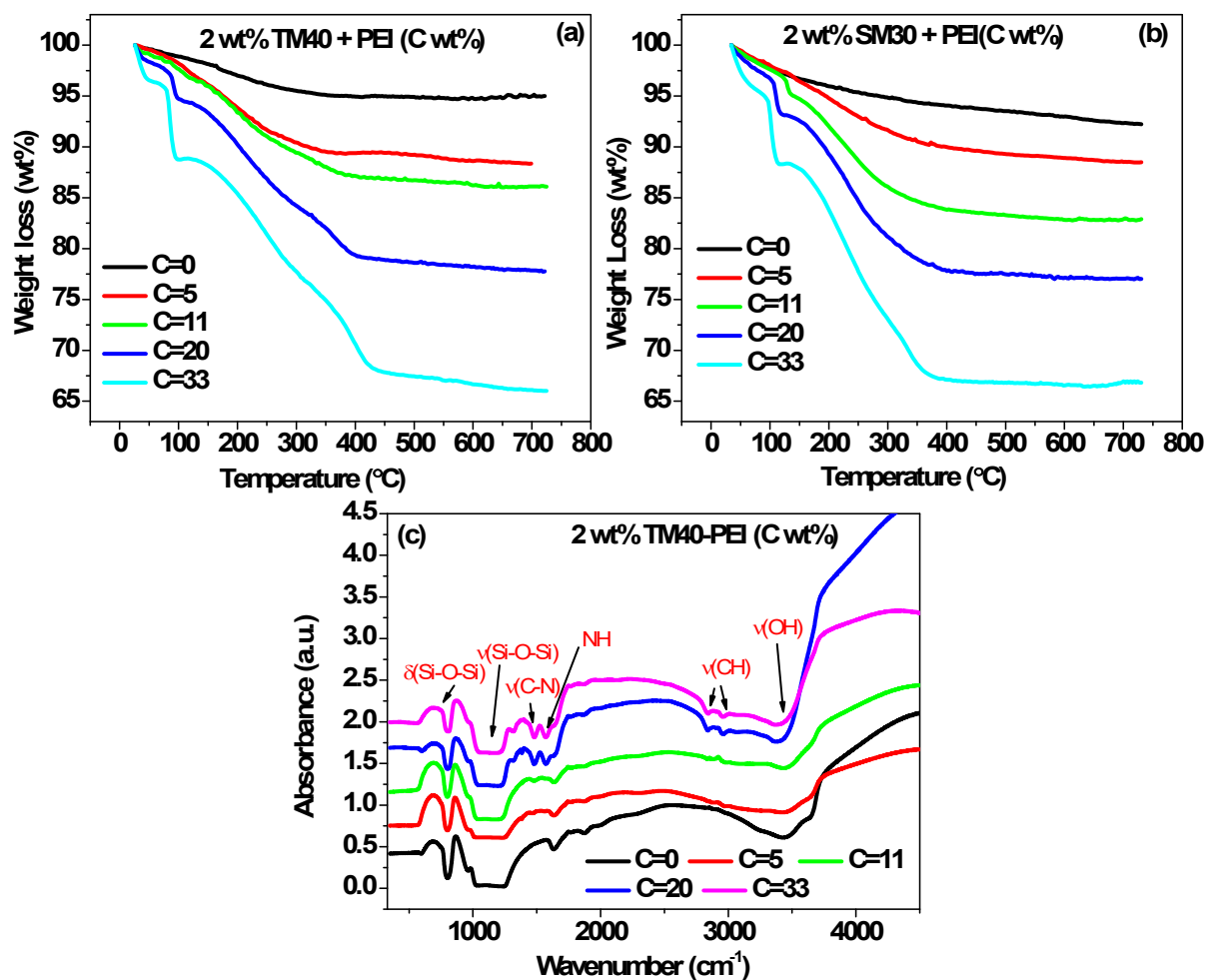

Figure S2: *(a)-(b) Thermogravimetric analysis and (c) FTIR spectra of supraparticles obtained at different PEI loadings.*

Thermogravimetric analysis (TGA) of the samples has been done using Linseis STA PT 1600. Before the measurements, samples were pre-treated in a 70 µL alumina pan at 100 °C for 1 hour in the air at ambient conditions to remove moisture from the samples. The samples were then cooled to room temperature and TGA measurements were taken. The estimated

concentration of PEI in the supraparticles corroborates with the experimental values of PEI used in the dispersion (Fig. S2a, b). Heat treatment of the samples upto 100 ˚C removes only free water. However, bound water cannot be removed completely.

Table S1: *Wt % loss in silica-PEI supraparticles as a function of PEI loading obtained from*

Sample	TM40	TM40-PEI(5)	TM40-PEI(11)	TM40-PEI(20)	TM40-PEI(33)
Wt % loss	6	12	14	23	33
Wt% bound water	6	7	3	3	-
Sample	SM30	SM30-PEI(5)	SM30-PEI(11)	SM30-PEI(20)	SM30-PEI(33)
Wt % loss	7	11	17	23	33
Wt% bound water	7	6	6	3	-

thermal stability measurements.

For pure silica supraparticles, ~ 6 % weight loss can be attributed to the release of bound water d silanol groups. However, weight loss in silica-PEI supraparticles has two contributions: (1) the release of the bound water and (2) the volatilization and decomposition of PEI. The contribution of the bound water is more at lower loading of PEI due to the porosity which results in trapping of the water in the interstices. At higher loading of PEI, due to the reduction in porosity, the contribution of bound water decreases. For PEI(33), the weight loss is due to the volatilization and decomposition of PEI as the excess of PEI fills the interstitial pores resulting in no bound water.

The infrared spectra of silica-PEI supraparticles have been recorded in the range 350-4500 cm^{-1} using a Bruker Vertex 80 V FTIR spectrometer under vacuum with an apodized resolution of 2 cm^{-1}. The Fourier Transform Infrared (FTIR) spectra of supraparticles with varying PEI concentrations are shown in Fig. S2c. The bands arising from the stretching and bending of the silanol groups are 800 cm^{-1} and 1090 cm^{-1}, respectively. The bands arising at 2847 cm^{-1} and 2943 cm^{-1} are attributed to the asymmetric and symmetric stretching vibrations of CH$_2$ at higher concentrations of PEI. The band arising at 1583 cm^{-1} is due to NH vibrations whereas the band at 1473 cm^{-1} is due to CN vibration existing at higher loadings of PEI. The bands from the stretching of -OH groups are observed at 3480 cm^{-1}. Thus, the presence of amine and carbon groups in the FTIR spectra and their subsequent increase with the increase in PEI loading confirms the PEI incorporation in the supraparticles.
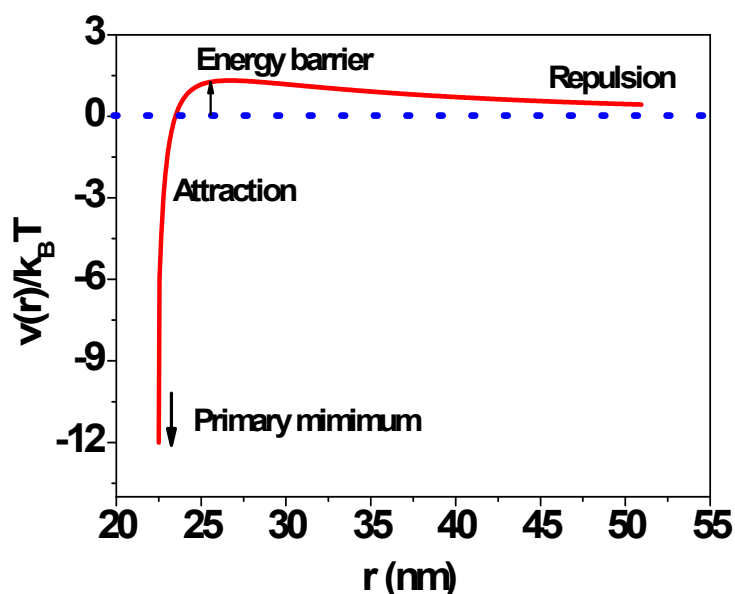
Interaction Potential

Figure S3: *DLVO interaction potential for silica colloidal dispersion (1 wt% TM40)*

The primary minimum along with the energy barrier in the interaction potential as shown below is included in the supporting information. It can be evidently seen that the nature of interaction among particles is contingent upon both their distance and thermal energy. When particles are

at a considerable distance and in a stable state, the predominant interaction is repulsion. As the particles approach each other, the potential increases, reaching its maximum at a specific distance between the particles. Subsequently, if the particles possess adequate energy to surmount the energy barrier, the interaction between them transitions to attraction, leading to bonding in the primary minimum. There are many external parameters which can reduce the energy barrier such as pH, ionic strength to mention a few.

In the case of pure silica dispersion as well as turbid region the potential has been calculated using DLVO (Derjaguin, Landau, Verwey and Overbeek) theory given as[1]:

$$\frac{U(r)}{k_BT} = -\frac{A_H}{6k_BT}\left\{\frac{d}{2r^2} + \frac{d^2}{2(r^2-d^2)} + \ln\left(1 - \frac{d^2}{r^2}\right)\right\} + Z^2\lambda_B\left(\frac{e^{\frac{\kappa d}{2}}}{1+\frac{\kappa d}{2}}\right)^2\left(\frac{e^{-kr}}{r}\right)$$

(1)

Here, A_H (2.4×10^{-21} J) is the Hamaker's constant for silica nanoparticles across the water. d is the diameter of the silica [TM40] nanoparticles, κ is the inverse of Debye length.

$$\kappa^{-1} = \left(\frac{e^2}{\epsilon_0\epsilon_r K_BT}\right)^{\frac{1}{2}}\sqrt{Z\rho + 2N_AI_s}$$

(2)

Here, e is the elementary charge, ρ is the particle number density, I_s is the ionic strength of the solution [10^{-4}-10^{-5} mol/L for the Millipore water], N_A is the Avogadro's constant. $Z = \pi\sigma_e d^2$ is the total charge of a particle with surface charge density σ_e. The surface charge density is calculated from measured Zeta potential. The Debye length is estimated to be ~ 50 nm [2] and it is assumed to be constant as addition of weak cationic PEI does not affect much the ionic strength of the dispersion.

$\lambda_B = e^2/4\pi\epsilon_0\epsilon_r k_BT$ is the Bjerrum length for water at 25 ˚C and is estimated to be equals 0.7 nm.

It has been shown earlier[3] that with the increase in the concentration of PEI there is a monotonic reduction in the energy barrier of the DLVO potential due to the aggregation of colloids in the intermediate region. However, the observed re-stabilization of silica-PEI dispersion at higher concentration of PEI could not be explained only by DLVO interaction potential as it does not account for the entropic forces due to PEI. The re-stabilization of silica-PEI dispersion at high concentration of PEI was attributed to the presence of free polymer mediated repulsion[4-6]. Therefore, in the high PEI concentration regime, the total interaction potential can be written as:

$$\frac{U(r)_{total}}{k_B T} = \frac{U(r)}{k_B T} + \frac{U(r)_{FPI}}{k_B T} \tag{3}$$

$$\frac{U(r)_{FPI}}{k_B T} = \frac{\pi}{2} d \int_r^\infty W(h) \, dh \tag{4}$$

$$W(h) = \frac{2\varkappa n C_b a^2}{R} \left\{ \frac{1}{h} - 0.75 - \frac{1}{h} + \frac{1}{\varkappa}\left(1 + \left[\frac{h}{2\varkappa} - 1\right]\ln\left[1 - \frac{2\varkappa}{h}\right]\right)\right\} \qquad \text{for } \frac{h}{R} < 1 \tag{5}$$

For $\frac{h}{R} > 1$, W(h) vanishes exponentially as $\dfrac{\exp\left(-\dfrac{h^2}{4}\right)}{h^4}$ [5]. Therefore, the free polymer induced repulsion has been estimated only for the region (h/R)<1.

Here, $a = a_s/\sqrt{6}$, a_s is the statistical segment length of the polymer. C_b is the bulk monomer concentration, n is the number of attractive sites in the polymer and $\varkappa$ is the relative thickness of the adsorbed polymer. For PEI with molecular weight 800 g/mol, the estimated value of the above parameters is as follows: a=0.2 nm, C_b=2.13 × 10^{21} g/cc, n=18 and $\varkappa$= 0.486.
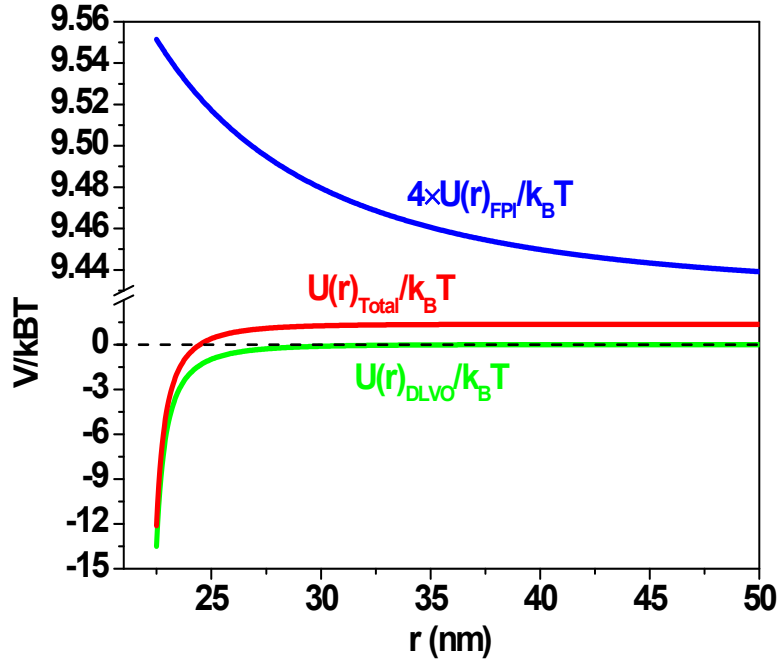
Figure S4: *Calculated interaction potential for 1 wt% TM40 + 10 wt% PEI representing the individual contribution of different terms along with the total interaction potential.*

Calculation for the drying time of the droplet

$$v = \frac{Q}{A} \tag{6}$$

Here v is the velocity of the colloidal droplet, Q is the aspiration rate and A is the area of the drying chamber.

$$\tau_{res} = \frac{L}{v} \tag{7}$$

Here, L is the length of the drying chamber.

The residence time of the colloidal droplet in the drying chamber has been calculated using eq. (6) and (7). The estimated τ_{res} is ~ 1.36 s.
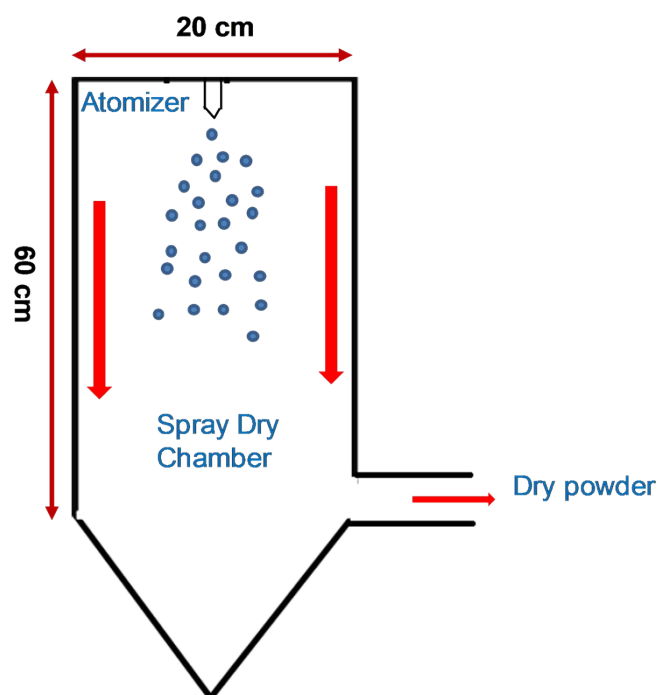
Figure S5: *Schematic of drying chamber of the spray dryer*
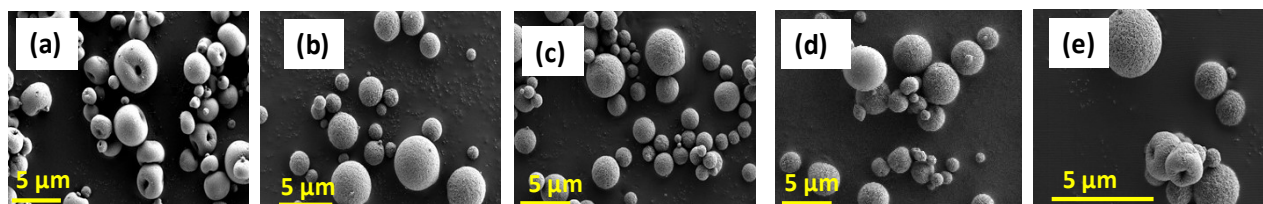
3. FESEM Analysis

Figure S6: *Low magnification electron microscopy images of (a) Si-PEI(0) (b) Si-PEI(5) (c) Si-PEI(11) (d) Si-PEI(20) (e) Si-PEI(33).*

The line-profile plot analysis of high-resolution FESEM images for silica-PEI supraparticles has been carried out using ImageJ software. This analysis involved plotting intensity as a function of distance across the image, the variations in intensity as a function of distance are observed, where high intensity indicates the presence of particles, and low intensity signifies empty spaces. To quantitatively assess this, the total count of white pixels (representing high

intensity) and black pixels (representing low intensity) in the image was calculated. Porosity

on the surface of the supraparticles was then determined using the formula:

$$Porosity = \frac{Total\ Black\ pixels}{Total\ white\ pixels + Total\ Black\ pixels} \quad (8)$$

The porosity for TM40-PEI supraparticles with the increase in the PEI loading is shown in the

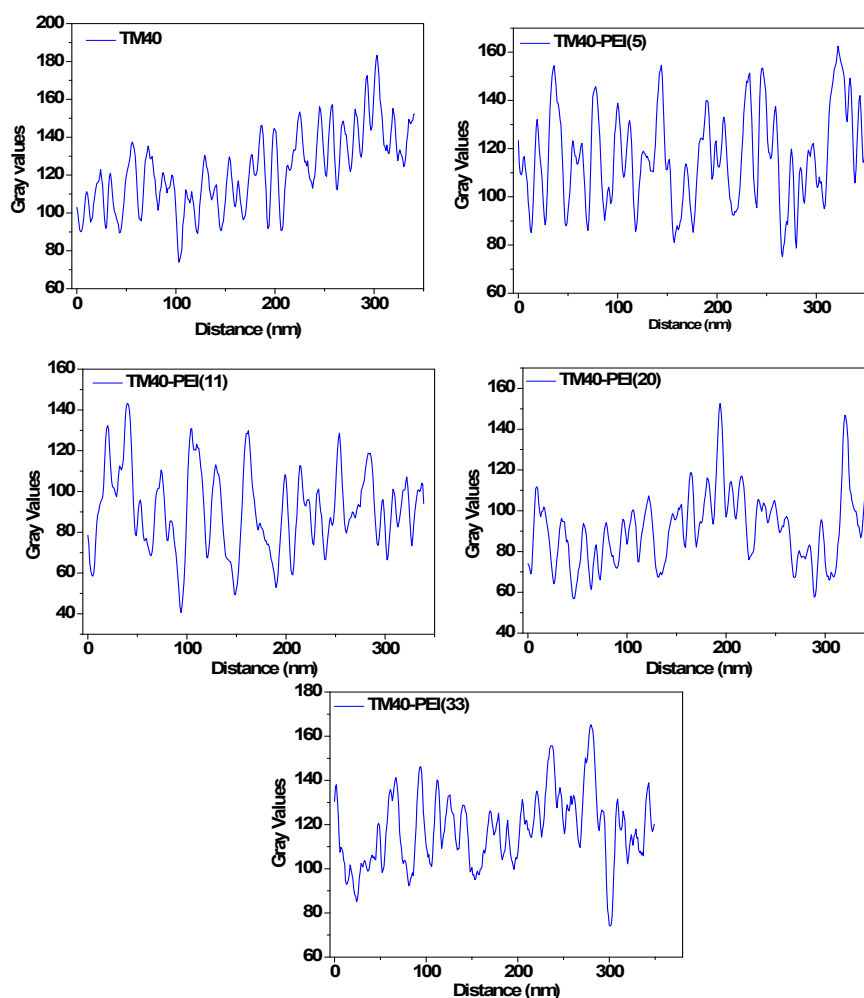Table S2 and the plot of the porosity as a function of PEI loading is shown in Fig. S8.

Figure S7: *Line profile plot analysis using ImageJ software of jammed TM40 colloids with PEI-assisted tuning of interaction.*

Table S2: *The variation in the porosity of TM40-PEI supraparticles as a function of PEI loading. The porosity has been obtained using high-resolution FESEM images of the supraparticles.*

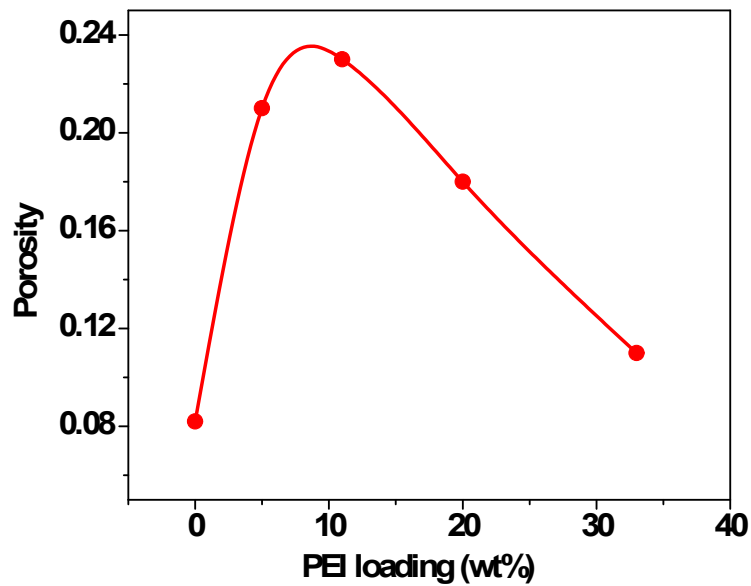| Sample Name	TM40	TM40-PEI(5)	TM40-PEI(11)	TM40-PEI(20)	TM40-PEI(33)
Porosity	0.089	0.21	0.23	0.18	0.11

Figure S8: *The variation in the surface porosity of jammed TM40 colloids with PEI-assisted tuning of interaction.*

4. SAXS Analysis

The scattering profiles [I(Q)] of the assembled supraparticles can be represented by the additive contributions from the correlated silica nanoparticles [$I_s(Q)$] and overall scattering from the supraparticles [7].

Thus, the total scattering intensity can be represented as:

$$I(Q) = I_s(Q) + \frac{C_{porod}}{Q^4} \qquad (9)$$

Here, $I_s(Q)$ is the scattering intensity from the silica colloids and the second term gives the scattering from the sharp interfaces modelled using Porod's law as the size of the supraparticles is large compared to the length scale probed by the SAXS, therefore, only surface scattering will be observed.

Due to the presence of the finite polydispersity in size, scattering intensity ($I_s(Q)$) under the local monodisperse approximation along with the weighted size distribution of the monodisperse subsystem is given as

$$I_s(Q) = \Delta\rho_{air-silica}^{2} \frac{\int D(r, r_0, \sigma)V(r)^2 P(Q,r)S(Q,r)dr}{\int D(r, r_0, \sigma)V(r)dr} \tag{10}$$

$D(r, r_0, \sigma)$ is the size distribution of the silica nanoparticles which is considered to be the log-normal distribution, given as [8] :

$$D(r, r_0, \sigma) = \frac{1}{\sqrt{2\pi r^2 \sigma^2}} e^{\dfrac{-\left[\ln\left(\dfrac{r}{r_0}\right)\right]^2}{2\sigma^2}} \tag{11}$$

Here, r_0 is the median radius and σ is the polydispersity index which varies in between 0 and 1. $P(Q,r)$ is the form factor which is taken as spherical because of the spherical shape of colloids given as [9]:

$$P(Q,r) = \left[\frac{3\{\sin(Qr) - Qr\cos(Qr)\}}{(Qr)^3}\right]^2 \tag{12}$$

$S(Q,r)$ is the structure factor which gives the information about the interparticle interactions[10]. Baxter's sticky hard sphere model has been used for the structure factor. In the sticky hard sphere model, the short-range attraction is accounted for by the square-well potential which is given as[11]:

$$\frac{V}{k_B T} = \begin{cases} \infty & r \leq d \\ \log\left(\frac{12\Delta\tau}{\Delta + d}\right) & d < r \leq d + \Delta \\ 0 & d > d + \Delta \end{cases} \tag{13}$$

Here, V is the square-well potential, T is the temperature, k_B is the Boltzmann's constant, Δ is the width of the well, d is the diameter of the silica colloids and τ represents stickiness in the system, a dimensionless quantity which is given as:

$$\tau = \frac{\Delta + d}{12\Delta}\exp\left(\frac{V}{k_B T}\right) \tag{14}$$

The sticky hard sphere structure factor is derived by solving the Ornstein-Zernike equation using square-well interaction potential and closure relation [10]. The analytical expression of S(Q,r) is given somewhere else [12].

The fitting has been done based on the non-linear least square method[13] using the software SASfit[14]. Lognormal size distribution along with spherical form factor has been taken as one contribution. And for the structure factor, sticky hard sphere model under local monodisperse approximation has been added as another contribution.
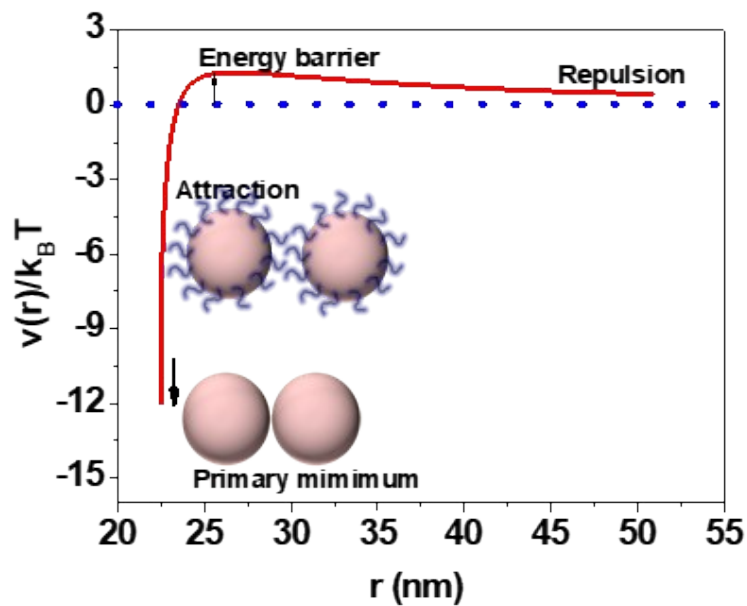
Figure S9: *Schematic for DLVO interaction Potential indicating the aggregation of bare colloids in primary minimum and flocculation of polymer adsorb colloidal particles before primary minimum at low attractive strength.*
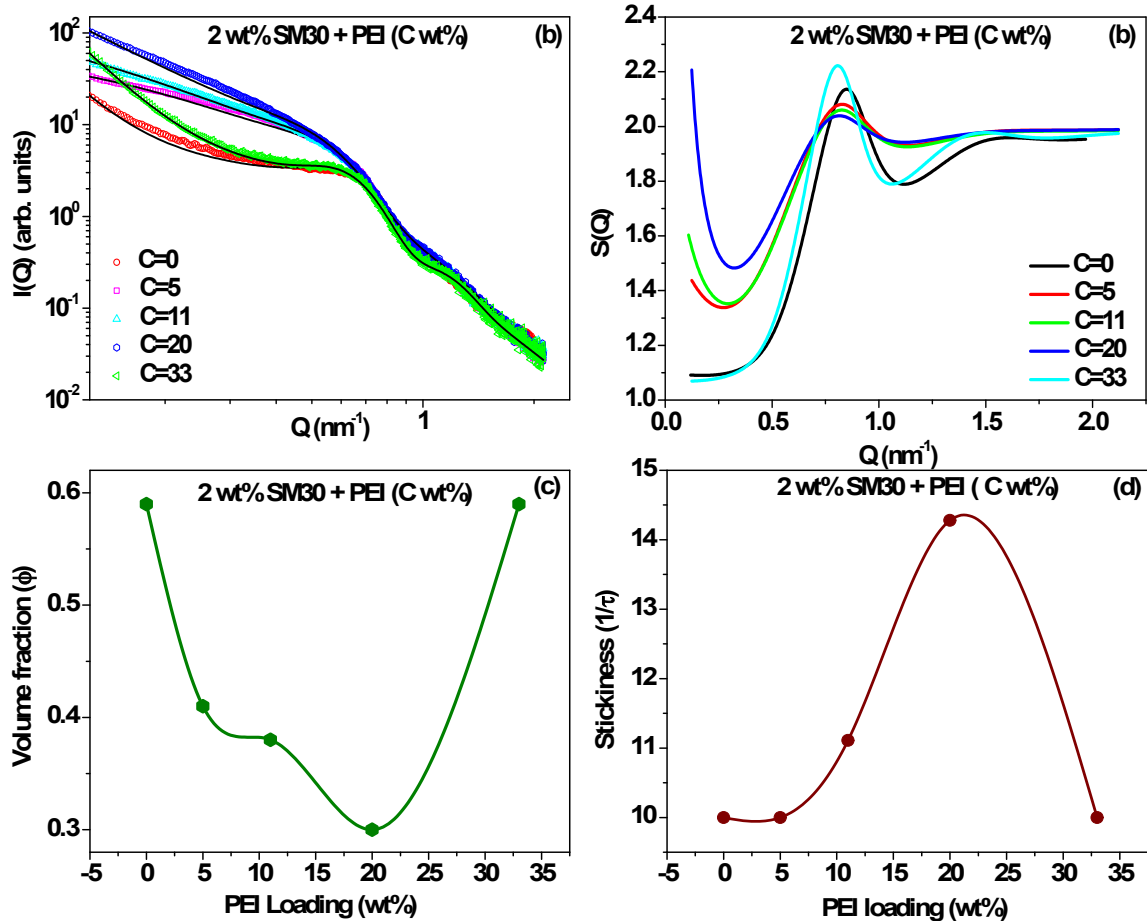

Figure S10: *(a) SAXS profiles for TM40-PEI supraparticles. Solid lines represent the non-linear least-square fit of the data. (b) Variation of the derived structure factor from the fitting of SAXS profiles (c) Variation in volume fraction (d) variation of dimensionless parameter, stickiness obtained from the fitting of the SAXS data as a function of PEI loading.*

5. Medium-Resolution Small-Angle Neutron Scattering (MSANS)

The silica-PEI supraparticle SANS measurements have been carried out using a double crystal monochromator-based SANS facility at Dhruva reactor, BARC, Mumbai[15]. The wavelength of the monochromatized neutron beam is 0.312 nm with a wavelength spread of ~ 1%. The final

SANS profiles have been corrected for the background as well as transmission with a Q-range of 0.0055 nm^{-1} to 0.173 nm^{-1}.
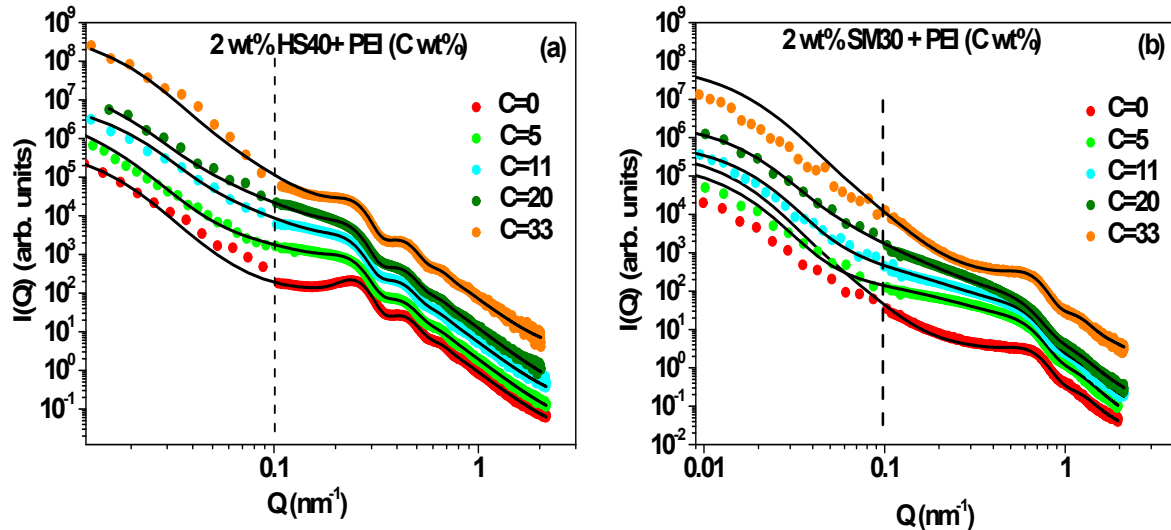

Figure S7: *The combined SANS/SAXS profiles for the (a) TM40-PEI and (b) SM30-PEI supraparticles obtained for different PEI concentrations. The solid line represents the fit of the data using two-length scale model. Data has been offset vertically for the clarity of the representation.*

The two-length scale model has been used for the fitting of the clubbed MSANS and SAXS data. For the fitting, an additional term has been incorporated. Now the $I_{total}(Q)$ is given as

$$I_{total}(Q) = I_S(Q) + \rho_{air-silica}^2 \frac{\int D(r, r_0, \sigma)V(r)^2 P(Q,r)dr}{\int D(r, r_0, \sigma)V(r)dr} \tag{15}$$

The contribution from the second term is coming due to the scattering from the overall supraparticles in the low-Q region. The MSANS data will give the information about the size of the supraparticles in the given Q-range. The fitting is done using SASfit software as explained above.

The size distribution obtained from the fitting of MSANS data is given below.
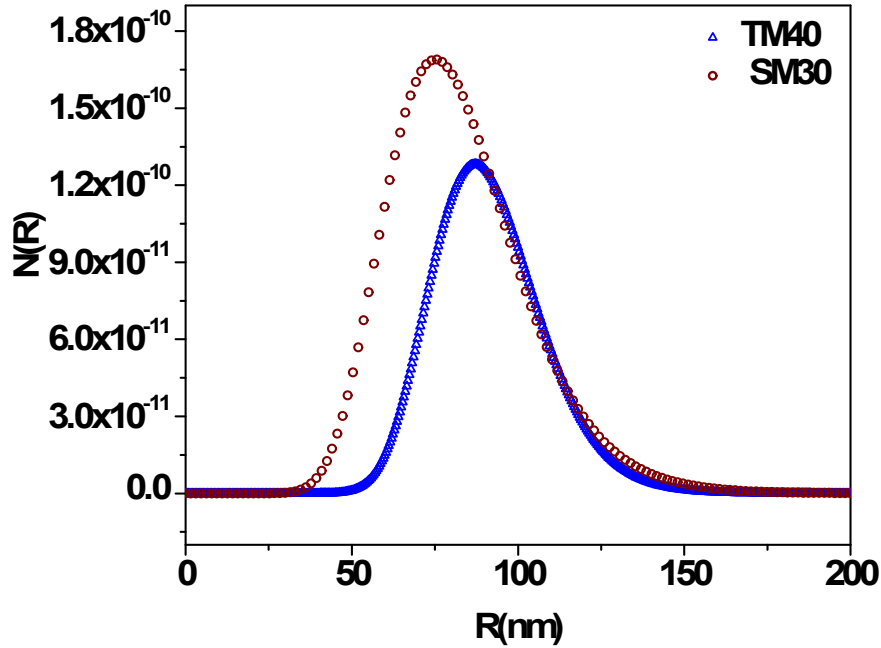
Figure S12: *The size distribution of SM30 and TM40 nanoparticles obtained via the model-dependent fitting of the MSANS profiles*

6. Positron Annihilation Lifetime Spectroscopy

A positron annihilation spectrometer of resolution ~ 175 ps consisting of two BaF_2 scintillation detectors coupled to a fast-fast coincidence circuit was utilized for positron lifetime measurements at room temperature. ^{22}Na radioisotope (~8μCi) sealed in polyimide envelope of an ~ thickness of 8 μm is used as positron source. The positron source was embedded in a sufficient amount of powder sample to ensure all the positrons annihilate within the sample. Samples are kept under a vacuum of 10^{-3} mbar at room temperature to acquire PALS spectra with a count greater than 1 million. The fraction of positron annihilating within the polyimide film is estimated by obtaining the PALS spectrum for silicon crystal under identical conditions.

To investigate the presence of supraparticles in porous materials positron annihilation lifetime spectroscopy is an established technique [16, 17] where the fraction of positrons implanted in the

porous materials form a bound state i.e., positronium with an electron. Due to the long intrinsic lifetime, the triplet state of positronium (ortho-positronium) annihilates through an additional mode of decay known as pick-off annihilation with electrons through the surface of pores. Thus, the pick-off annihilation time of the ortho-positronium and corresponding intensity provide quantitative information regarding the pore size and their density in the porous materials.
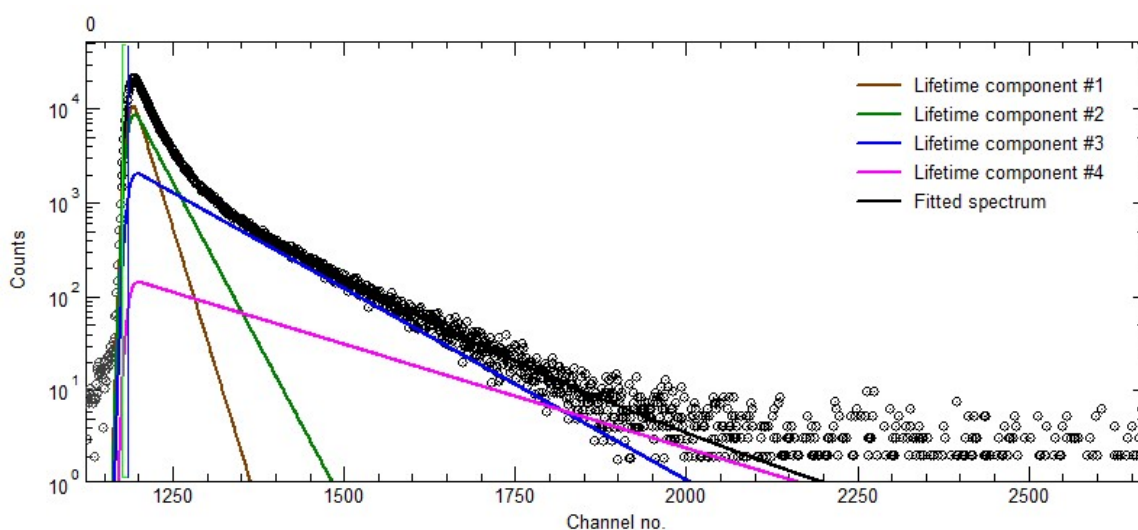

Figure S13: *Positron Annihilation Lifetime Spectrum for TM40-PEI(20) supraparticles. The Solid lines represent the fitting of the PALS lifetime components using PALSFit3.*

The positron annihilation lifetime spectroscopy spectrum for TM40-PEI supraparticles for 20 wt% loading of PEI is shown in Fig.S8. The long ortho-positronium indicates the signature of micro-porosity present in the supraparticles. The discrete positron lifetime components are analyzed using PALSFit3 [18]. The positronium lifetime in increasing order is attributed to para-positronium, free positronium, and ortho-positronium respectively where only ortho-positronium provides the information regarding the porosity in the silica-PEI supraparticles.

Table S3: *The ortho-positronium lifetime and intensity of the SM30-PEI supraparticles obtained via fitting of the PALS spectra using PALSFit3.*

SM30-PEI(C wt%)	$\tau_3 (\pm 0.003)$, ns	$I_3 (\pm 0.22)$, %	$\tau_4 (\pm 0.35)$, ns	$I_4 (\pm 0.03)$, %
0	1.343	25.02	12.48	1.15
5	1.071	25.70	14.66	2.23
11	1.105	28.22	14.34	2.58
20	1.113	30.35	15.36	2.59
33	1.211	34.19	9.45	1.02

Table S4: *The ortho-positronium lifetime and intensity of the TM40-PEI supraparticles obtained via fitting of the PALS spectra using PALSFit3.*

TM40-PEI(C wt%)	$\tau_3 (\pm 0.003)$, ns	$I_3 (\pm 0.22)$, %	$\tau_4 (\pm 0.35)$, ns	$I_4 (\pm 0.03)$, %
0	1.438	20.56	11.03	1.16
5	1.349	20.70	8.818	1.80
11	1.346	22.95	7.650	1.77
20	1.402	26.61	6.814	1.144
33	1.630	20.13	NA	NA

The ortho-positronium lifetime and their corresponding intensity for both TM40-PEI and SM30-PEI supraparticles are shown in Table S3 and S4 respectively. The existence of two distinct ortho-positronium lifetime components (τ_3 and τ_4) confirms the presence of two different sizes of pores in the silica-PEI supraparticles. The alteration in the ortho-positronium lifetime components with the increase in PEI loading can be attributed to the presence of PEI chains at the pore sites. Therefore, the pore sizes with the variation in the PEI loading are calculated using the Tao-Eldrup equation, given as [19, 20]:

$$\frac{1}{\tau_{po}} = 2\left[1 - \frac{R}{R + \Delta R} + \frac{1}{2\pi}\sin\left(\frac{2\pi R}{R + \Delta R}\right)\right]$$

(16)

Here, τ_{po} (ns) is ortho-positronium pick-off lifetime, R (nm) is the radius of the pore and ΔR is electron surface layer thickness ~ 0.166 nm.

The jamming of the silica nanoparticles in the silica-PEI supraparticles with the variation in the PEI loading can lead to the formation of the hierarchical pore network with the presence of both mesopores as well as micropores. In our previous work, the presence of the mesopores in the silica-PEI supraparticles had been characterized by utilizing N_2 adsorption-desorption isotherm [3]. However, this technique cannot detect pores of size less than the size of an N_2 molecule. Therefore, to establish the presence of micropores in the silica-PEI supraparticles Positron Annihilation Lifetime Spectroscopy (PALS) has been employed. The lifetime of o-Ps provides information about the porosity in the supraparticles and the existence of two distinct lifetimes of o-Ps (τ_3 and τ_4) reveals the presence of pores having two distinct sizes.

The pore sizes corresponding to the ortho-positronium lifetime component, τ_3, and τ_4 for both silica-PEI supraparticles are shown in Fig. 6a and b respectively. The size of pores corresponding to both lifetimes is less than 20 Å indicating the pores to be micropores. The pore size corresponding to τ_3 lifetime component of pure TM40 supraparticles is larger compared to pure SM30 supraparticles as the size of colloidal particles of TM40 is larger resulting in the large interstices due to the jamming of colloids. However, for the PEI loading of 5 wt%, the pore size of both the silica-PEI supraparticles has been reduced as the PEI molecules are hereby now tethered on the silica colloids due to the adsorption of PEI on the surface of silica nanoparticles which leads to a small decrease in the pore size. The ortho-positronium intensity (τ_3 lifetime component) for both silica-PEI(5) supraparticles [Table S3 and S4] remains identical to their respective pure silica supraparticles suggesting that the tethered PEI molecules occupy the smaller pores existing in the supraparticles without altering the arrangement of silica colloids within the supraparticles. Further increase in the PEI loading

till 33 wt% results in the increase in the pore size where the pore size of TM40-PEI(33) microgranules is larger than the bare supraparticles implying the alteration in the packing of the silica colloids within the supraparticles due to the tethering of PEI chains. Ortho-positronium intensity [Table S3 and S4 in the supporting information] increases beyond the pure silica supraparticles with the increase in the PEI loading. The positronium formed in the bulk of the porous supraparticles diffuses to pores driven by zero-point energy. Therefore, the enhancement in the o-Ps intensity in the silica-PEI supraparticles with the increase in the PEI loading suggests the diffusion of the positronium in the PEI layer adsorbed on the surface of silica colloids. The variation in the pore size as well as in the ortho-positronium intensity with the increase in the PEI loading attributed to the modification in the jamming of the silica nanoparticles in the silica-PEI supraparticles as well as the dynamics of the PEI chains tethered to the silica colloids.

The variation in the pore size corresponding to a longer ortho-positronium lifetime ($^{\tau}4$) is shown in Fig. 6b. Contrary to the smaller size pores [shown in Fig 6a], the size of the larger size pores decreases with the increase in the PEI loading. The size of the pores for TM40-PEI(33) supraparticles cannot be observed using a positron as the probe indicates that microporosity is dominated by PEI molecules within the supraparticles due to the high loading of PEI. A decrease in the intensity of the o-Ps for both the silica-PEI supraparticles at high PEI loading further confirms that the dynamics of the PEI layer present on the silica colloids defines the microporosity in the supraparticles particularly at higher loadings of PEI.

7. Broadband Dielectric Spectroscopy

7.1 Relaxation dynamics of PEI embedded in silica supraparticles

Dielectric measurements with varying temperatures have been carried out in a temperature range of 180 - 300 K using an Impedance analyzer from Novo Control, Germany. The

temperature during the measurements is controlled using the Quatro Cryo system (within ±0.5 °C). The measurements have been carried out in a wide frequency range of 0.1–1×10^7 Hz applying AC voltage 0.1 V. All the measurements have been carried out on powder samples using a standard sample holder provided by Novocontrol. It is to be noted that BDS measurements were carried out after heating the samples for 2 hours under vacuum (10^{-3} mbar) at ~100°C to remove the adsorbed water from the supraparticles and bulk PEI. A detailed study on the interplay between pore network modifications and dynamics of PEI in SM30-based supraparticles has been published as Ref [21]

7.2 Results and Discussion

Figure S14 shows the temperature-dependent variation of the imaginary component (ε") of the complex permittivity (ε*) of TM40-PEI(11) samples. Similar data have been obtained for all the samples including bulk PEI. A significant variation is observed in the loss permittivity (ε") as a function of temperature. At high temperatures (~ 300 K), a peak at higher frequency followed by a flank in a low-frequency region is observed in ε" variation with frequency [shown by the individual contribution of the fitting curve, Fig. S15] The conductivity term contributes in the low frequency region whereas HN1 and HN2 attributes to the two segmental relaxations corresponding to PEI present in the core as well as at the interfaces. Thus, the peak in the data corresponds to the segmental relaxation. On decreasing the temperature, the peak is observed to shift to lower frequencies [marked by arrow] with the appearance of additional peaks corresponding to relaxations with the interphase layer as well as secondary (beta) relaxations. Figure 7 in the main manuscript shows the effect of confinement on PEI dynamics in SM30 and TM40 silica-based supraparticles through loss permittivity (ε") variation with frequency at 250 K. At 250 K, segmental relaxations corresponding to PEI existing at the interphase region and in the core of pores are present in the frequency window of the instrument used for the measurements.
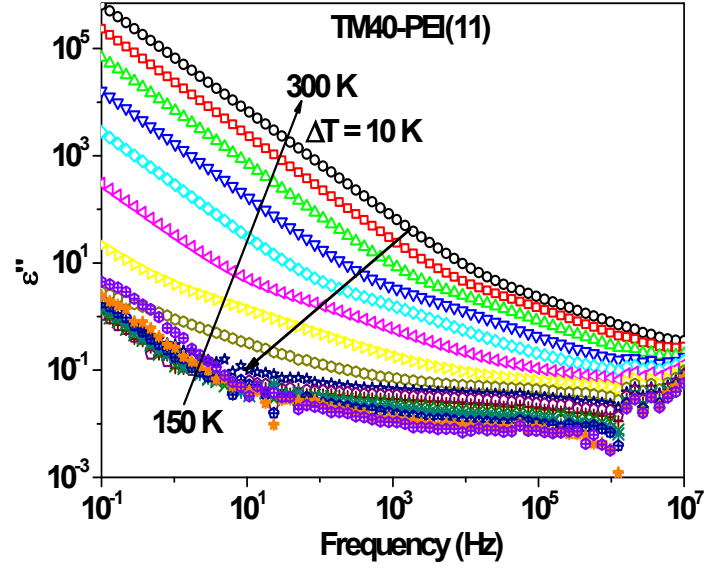
Figure S14: *Frequency-dependent loss permittivity of PEI-12.5 TM40 in the temperature range 150-300 K with a temperature interval of 10 K.*

The relaxation times corresponding to segmental relaxation of PEI in the core of the pores or at the interphase have been evaluated by analyzing the dielectric loss (ε'') data as a sum of Havriliak-Negami (HN) functions (depending on the peaks present) and an expression accounting for ionic conductivity seen as the flank in lower frequency region [eq. 17]

$$\varepsilon'' = \varepsilon_\infty + \sum_i^k \left\{ \frac{\Delta\varepsilon}{[1+(i\omega\tau_{HN})^\beta]^\gamma} \right\} - i\left(\frac{\sigma_0}{\varepsilon_0\omega} \right)^s \qquad (17)$$

where ε'', ε_0, ε_∞, $\Delta\varepsilon$, and τ_{HN} are the complex dielectric permittivity function, the dielectric permittivity of vacuum, the permittivity of the unrelaxed medium, the dielectric strength and the characteristics relaxation time corresponding to a different number (k) of relaxation processes. The parameters β and γ are the shape parameters (range 0-1) corresponding to the symmetric and asymmetric broadening of the HN functions defining the relaxation process. The parameter $\omega = 2\pi f$ is the angular frequency of the applied electric field and $0 < S < 1$ is the

scaling parameter. The dielectric spectroscopy data shown in Fig. 7 [main manuscript] has been fitted using eq. (17). k signifies the number of segmental relaxations. Here, k has been selected one or two to effectively model ε" when one or two segmental relaxations corresponding to the PEI in the core or interface as well as both are considered. The fit of the data results from the combined contributions of the conductivity term and segmental relaxations. The distinct contribution of the each of these terms in the fitting process is shown in Fig. S15.   The segmental relaxation times of PEI at the interphase region and in the core of the pores are given in Table S5.
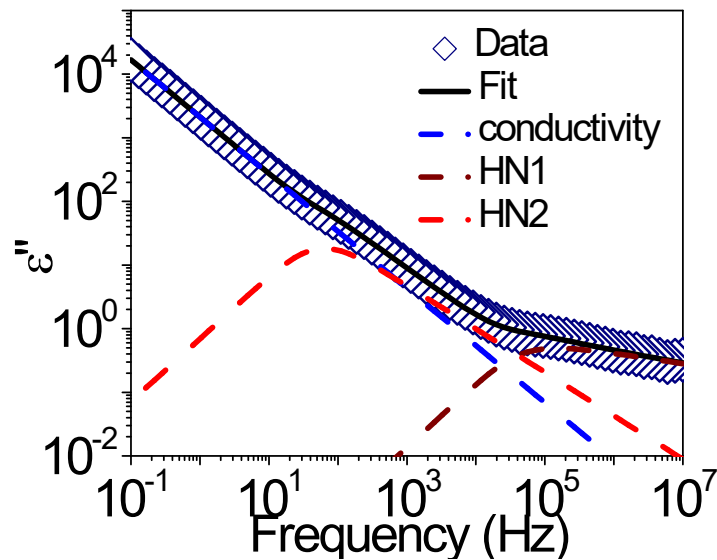

Fig. S15: *Frequency dependent loss permittivity (ε") for silica-PEI supraparticles. Solid line represents the complete fit of the data. Dashed lines show the individual contribution of the terms in eq. (6).*

All the relaxation times are longer than that of bulk PEI confirming that segmental motion of PEI under confinement is slowed down. In the case of all the TM40-based supraparticles, a distinct much slower relaxation process attributed to the PEI at the interphase region is present along with the segmental relaxation process of PEI from the core of the pores. The segmental

relaxation of PEI corresponding to interphase region becomes slower with the decrease in PEI loading in the TM 40 based supraparticles due to enhanced interaction of PEI with the silica nanoparticles surface. In the case of SM30-based supraparticles, the relaxation process corresponding to the interphase region is present in the experimental frequency window only for the low loading of PEIs. The segmental relaxation corresponding to PEI from the core region of pores does not vary linearly with PEI loading in the supraparticles. It indicates that due to the non-monotonic jamming of the silica nanoparticles in the supraparticles, distinct pore architecture evolved during the evaporation assembly of the nanoparticles. As a result, pore architecture at different PEI loading which acts as the confining media for PEI, relaxation processes of PEI under confinement in these supraparticles vary non-monotonically.

Table S5: *-log ($\tau_{s,1}$) and -log ($\tau_{s,2}$) corresponding to segmental relaxation of PEI in the core region of the pores and at interphase in the silica nanoparticles (SM30 and TM40) based supraparticles, respectively at 250 K.*

Sample	-log ($\tau_{s,1}$ sec)	-log ($\tau_{s,2}$ sec)
Bulk PEI	6.904	---
TM40-PEI(5)	3.202	1.129
TM40-PEI(11)	5.626	2.076
TM40-PEI(20)	5.104	2.648
TM40-PEI(33)	5.389	2.766
SM30-PEI(5)	3.348	-1.265
SM30-PEI(11)	1.871	-1.237
SM30-PEI(20)	3.160	
SM30-PEI(33)	2.279	

References

1.   S. Kumar, I. Yadav, S. Abbas, V. K. Aswal and J. Kohlbrecher, *J Physical Review E*, 2017, **96**, 060602.
2.   Y. Zeng, S. Grandner, C. L. Oliveira, A. F. Thünemann, O. Paris, J. S. Pedersen, S. H. Klapp and R. von Klitzing, *Soft Matter*, 2011, **7**, 10899-10909.
3.   S. Mehta, J. Bahadur, D. Sen, S. Singh and V. Polshettiwar, *Soft Matter*, 2022, **18**, 5114-5125.
4.   D. H. J. Napper, *Polymeric stabilization of colloidal dispersions*, Academics, London, 1983.
5.   A. Semenov and A. Shvets, *Soft Matter*, 2015, **11**, 8863-8878.

6.   A. Shvets and A. Semenov, *Journal of chemical physics*, 2013, **139**.
7.   A. Guinier, G. Fournet and K. L. Yudowitch, *Small-Angle Scattering of X-rays*, Wiley, New York, 1955.
8.   J. Aitchison and J. A. C. Brown, *The Lognormal Distribution*, University Cambridge Press, New York, 1969.
9.   Y. B. Melnichenko, *Small-Angle Scattering from Con Ned and Interfacial Fluids*, Springer, 2016.
10.   S. Menon, C. Manohar and K. S. Rao, *The Journal of Chemical Physics*, 1991, **95**, 9186-9190.
11.   R. Baxter, *The Journal of Chemical Physics*, 1968, **49**, 2770-2774.
12.   A. Chinchalikar, V. Aswal, J. Kohlbrecher and A. Wagh, *J Chemical Physics Letters*, 2012, **542**, 74-80.
13.   J. S. Pedersen, *J Advances in colloid interface science*, 1997, **70**, 171-210.
14.   I. Breßler, J. Kohlbrecher and A. F. Thünemann, *J Journal of applied crystallography*, 2015, **48**, 1587-1598.
15.   S. Mazumder, D. Sen, T. Saravanan and P. Vijayaraghavan, *Current Science*, 2001, **81**, 257-262.
16.   T. Ahn, D. W. Gidley, A. W. Thornton, A. G. Wong-Foy, B. G. Orr, K. M. Kozloff and M. M. Banaszak Holl, *ACS nano*, 2021, **15**, 4321-4334.
17.   S. Sharma, P. Utpalla, J. Bahadur, A. Das, J. Prakash and P. Pujari, *The Journal of Physical Chemistry C*, 2020, **124**, 25291-25298.
18.   P. Kirkegaard and M. Eldrup, *Computer Physics Communications*, 1972, **3**, 240-255.
19.   M. Eldrup, D. Lightbody and J. N. Sherwood, *Chemical Physics*, 1981, **63**, 51-58.
20.   S. Tao, *The Journal of Chemical Physics*, 1972, **56**, 5499-5510.
21.   S. K. Sharma, S. Mehta, P. Utpalla, M. Sahu and J. Bahadur *Journal of Physical Chemistry C*, 2023*, **127,** 10197–10206, .